

# We are IntechOpen, the world's leading publisher of Open Access books Built by scientists, for scientists

6,900

Open access books available

186,000

International authors and editors

200M

Downloads

Our authors are among the

154

Countries delivered to

TOP 1%

most cited scientists

12.2%

Contributors from top 500 universities



WEB OF SCIENCE™

Selection of our books indexed in the Book Citation Index  
in Web of Science™ Core Collection (BKCI)

Interested in publishing with us?  
Contact [book.department@intechopen.com](mailto:book.department@intechopen.com)

Numbers displayed above are based on latest data collected.  
For more information visit [www.intechopen.com](http://www.intechopen.com)



# The LDV and PIV Study of Co-Rotating Disks Flow with Closed Shroud

Shen-Chun Wu\*

*Department of Aviation Mechanical Engineering,  
China University of Science And Technology, Taipei,  
Taiwan*

## 1. Introduction

The co-rotating disks system is applied to a wide range of industrial machinery. This study focuses on co-rotating disks of magnetic disk storage devices. Although numerous experimental and numerical studies have been given to the relevant flow field, the flow physics has not been completely elucidated as a result of its inherent complexity. Consequently, investigating the flow field in detail is required. Many studies have analyzed this flow type; however, for the sake of brevity, only the most relevant works are cited in this work.

Stewartson (1953) first investigated flow between un-shrouded co-rotating disks using theoretical analysis combined with flow visualization and obtained an analytic solution. However, variation in experimental parameters and detailed experimental data were lacking. Lennemann (1974) performed experiments in water to visualize flow between co-rotating disks. Using aluminum particles as light scattering agents, Lennemann visualized a laminar core of fluid extending from the hub to the periphery of the disks that rotated at about 80% of the disk rotation speed. Szeri et al. (1983) examined flow between un-shrouded co-rotating disks in detail. Laser Doppler Velocimetry (LDV) was employed in measuring only circumferential and radial velocities. The measured velocity profile indicated that fluid exists in solid body rotation. Also using LDV, Chang et al. (1989) determined the mean velocity and root mean square value of velocity fluctuation. One year later, Chang et al. (1990) investigated this flow numerically. Abrahamson et al. (1988, 1989) utilized a hot film probe to measure velocity spectra. Their experimental results indicated that the spectra converged at a single frequency. The peak energy at integral normalized frequency was obtained by dividing the measured spectra frequency by 75% of the rotating speed of the disks. The authors also utilized added bromothymol blue to co-rotating disk water to clearly show that the polygon shapes were correlated with circumferentially periodic and axially aligned flow vorticity. Schuler et al. (1990), who also employed LDV to measure the co-rotating flow in an enclosure, elucidated the solid body rotation region near the hub. Their power spectra analysis results were in agreement with those obtained by Abrahamson; however, their study presented only one measured point. Tzeng and Humphrey (1991) measured the flow between shrouded co-

---

\* Corresponding Author

rotating disks using the LDV technique in airflow. The velocity time sequence had distinct sinusoidal-like oscillations. Humphrey and Gor (1993) visualized the flow between disks in an experimental apparatus similar to that used by Schuler et al. by illuminating micro-sized mineral oil droplets on a laser sheet. Humphrey et al. (1995) numerically analyzed the unsteady flow motion utilizing a time-explicit algorithm. Iglesias and Humphrey (1998) confirmed the existence of a symmetrical pair of counter-rotating vortices in the cross-stream ( $r$ - $z$ ) plane via numerical results. Herrero et al. (1999) continued this line of research. Randriamampianina et al. (2001) carried further analyzed co-rotating disk flow numerically. Wu and Chen (2002) examined large-scale structures between shrouded co-rotating disks. Two LDVs and a phase-averaged technique scheme were applied to examine the coherent structures. Based on reconstructed streamline patterns, three distinct flow regions were quantitatively identified. Using the same apparatus and technique, Wu and Chen (2003) examined shrouded co-rotating disks, and measured density points that were four times of that obtained one year before. The measured instantaneous velocity (phase-averaged) fluctuations were also applied to calculate Reynolds stresses for exploring turbulent flow dynamics. Wu et al. (2006) examined the flow between a pair of enclosed co-rotating disks using LDV. A systematic measurement with wide  $Re$  ranging from  $10^4$  to  $10^6$  was conducted, and the effect of  $Re$  on the flow structure was investigated. They performed a power spectra analysis and developed an equation for calculating the number of outer region vortices. Wu, (2009) examined the coherent flow between enclosed co-rotating disks using PIV. The core region revealed that a pair of circular flow structure acts like an annular chain to surround the large-scale vortex. This finding was not reported in the literature.

Flow visualization techniques (Lennemann et al., 1974; Abrahamson et al., 1989; Humphrey and Gor, 1993) or point-wise velocity measurements (Chang et al., 1989; Schuler et al., 1990; Wu and Chen, 2002, 2003; Wu et al., 2006; Wu, 2009) were applied in early experimental studies. However, a complete experiment conducted in both the  $r$ - $\theta$  plane and the  $r$ - $z$  plane was still not found. Point-wise experimental techniques, such as LDV or Hot Wire Anemometer (HWA), were limited to acquiring time-averaged velocity. Although phase-averaged measurement results were obtained, those results were not instantaneous. Thus, the present effort attempts to complement this work with planar velocity measurements via PIV, permitting structural and instantaneous interpretation of the kinematical behavior for this flow type. PIV reveals instantaneously and quantitatively the global structures in a two-dimensional or three-dimensional flow field without disturbing the flow, and are extremely effective and necessary. Consequently, this work utilizes the LDV and PIV technique. In addition, flow visualization image in each plane is employed to examine the flow structure established based on the velocity measurements.

## 2. Experimental method and apparatus

In this work the parameters of a 3.5-inch hard disk are adopted as the reference to determine the dimensions of the test configuration and the values of the relevant flow parameters for the enclosure co-rotating disk pair flow via dynamic similarity.

### 2.1 Flow facility

Fig. 1 schematically depicts the investigated geometry. The experimental model comprised a motorized test section fixed to an inertial test stand. Two rigid disks were concentrically

clamped to a hub. The disks were made of transparent Plexiglas and had a thickness of 10mm. The spacer (D) measuring 17.4mm in diameter and having a radius of  $R_1=59.4$ mm, was used to separate the disks in the spindle axis direction (z direction). Measurements were performed at the middle of the test section. The test section shroud was also made of transparent Plexiglas with an axisymmetric inner wall and a radius of  $R_3 = R_2 + a = 189.5$ mm. Flow visualization in the  $r-\theta$  plane was also limited to the inter-disk mid-plane. In this work, dimensionless axial distance of disks was set at  $S = 0.09$ , and the Reynolds number was  $Re = 5.25 \times 10^5$ . The values of  $Re$  and  $S$  correspond to the rotation speed of about 12000 rpm for the next generation hard disk and general disk space. An approximate dynamic similarity is ensured by setting  $Re_{(model, water 30^\circ C)} = Re_{(prototype, air 30^\circ C)}$ . Pure water was utilized as the working fluid to attain high Reynolds number at relatively low model disk rotation speed of  $\Omega = 133$ rpm.

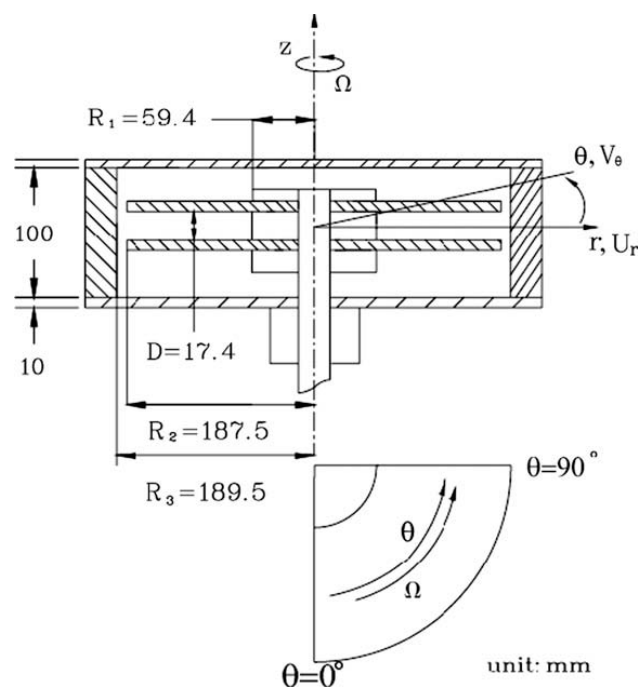


Fig. 1. Sketch of configuration coordinate system and of the test section.

## 2.2 LDV system

The principle and practice of LDV have been introduced elsewhere, e.g. Durst et al. (1981). The LDV systems with direct relevance to the present study are introduced here. Two laser velocimeters, an LDV and a Phase Doppler Particle Analyzer (PDPA), were utilized in order to carry out phase-averaged measurements. The schematic of the optical arrangement is shown in Fig. 2. The two component fiber-optic LDV system worked in a forward scattering mode during the measurements. The optical module consisted of the following components: a TSI Model 9201 Colorburst Multicolor Beam Separator, four Model 9271 couplers, an argon-ion laser (Coherent Innova 90, 2W), a probe with front collimating lens of 350 mm focal length, a single-mode polarization-preserving fiber, a Bragg cell, two pinhole filters and two photomultiplier optics sections. The associated electronics included two photomultipliers, two electronic frequency shifters, three TSI 1990C counter processors, a TSI-MI990 buffer interface. The PDPA system consisted of five major components:

transmitter, receiver, signal processor, motor controller box, and a computer. The Aerometrics model XMT-1100-4S transmitter was used to generate two equal intensity laser beams and to focus them to an intersection point that formed the measurement region. The transmitters contained a Spectra-Physics model SP-106, 10mW, and polarized helium-neon laser. Optical components within the transmitter served to focus, partition, and collimate the laser beam. A beamsplitter with radial diffraction grating helped to produce a frequency shift on measured particle signals. The Aerometrics model MCB-7100-1 motor controller was used to monitor and control the frequency shift. The receiver model RCV-2100 collected the light scattered from seeding particles. The receiver was then connected to the PDP-3100 signal processor with 2  $\mu$ s resolution to process the Doppler signals. The analog output of the PDP-3100 signal processor was transmitted to the TSI counter processor. Pure water was used as the working fluid in the experiment. MgO particles with a diameter of about 1.2  $\mu$ m, were adopted as seeding material in the LDV measurements.

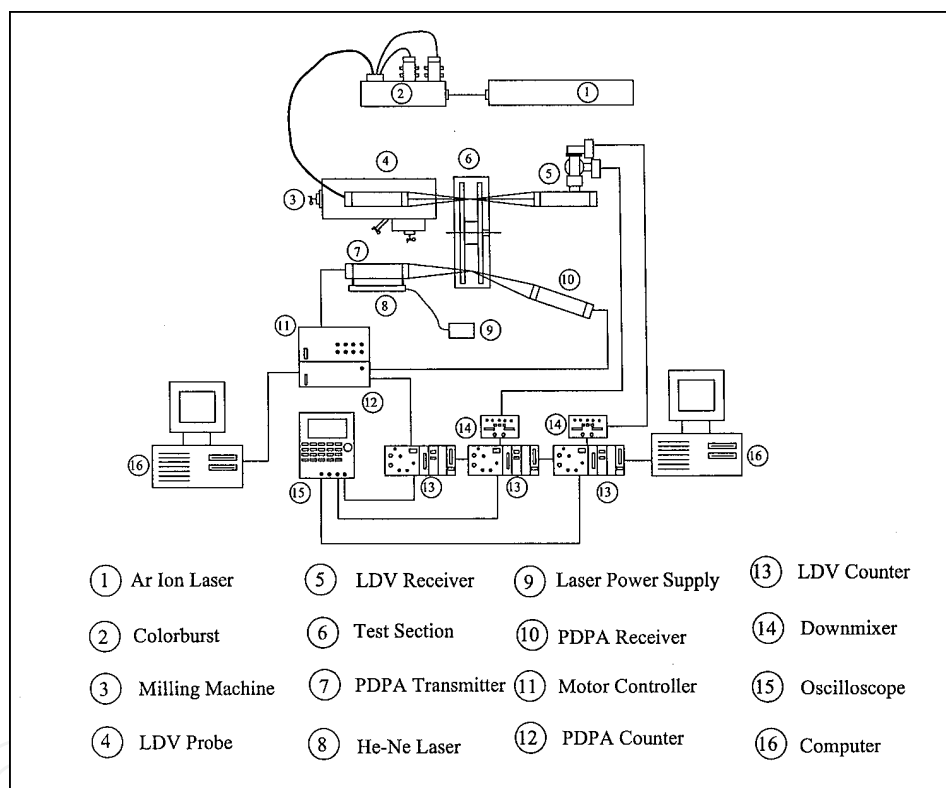


Fig. 2. Sketch of LDV experimental apparatus.

### 3. Measurement technique and data reduction

During the measurements, the PDPA probe was fixed at a specific position ( $r^*=0.75$ ,  $Z/H=0.5$ ) where the circumferential velocity power spectra had peak values. To investigate the vortical structures, all of the LDV measurements were made in a quarter of the center plane between the two co-rotating disks. In the measurement domain there were totally 4096 points. The PDPA probe was kept at the specific position as phase reference while the LDV probe was translated in the measurement domain by a three-axis translation stage with an uncertainty of 0.02 mm. Doppler burst signals detected from PDPA and LDV were transferred to the LDV counters, which worked in coincident mode under the control of the

TSI MI-990 interface module. A coincident time window length (0.1 ms) was set in the MI-990 interface module to test the synchronization of burst signals detected by PDPA and LDV. The burst signals were processed to compute the Doppler shift frequency, as the time intervals of signals detected by PDPA and LDV were lower than the coincident time window length. Data of Doppler shift frequency was then transferred to a personal computer via a DMA interface card. The velocity values were further calculated and then the time sequence was stored. The coincident data rate was kept at about 2000 Hz as the measurement was made, which was high enough to resolve the periodic motion of vortical structure with 5.08Hz of frequency in the present study. In each measurement, more than 20,000 samples of time sequences of reference point and measuring points were collected, respectively. All of the time histograms of velocity, whether circumferential or radial component, were measured with respect to the same phase reference point. Measurement examples using the phase-averaged method are shown in Fig. 3. A cycle was built between two adjacent crests of time series of  $U_{ref}$ , and was then divided into ten phases of equal time interval with phase one and phase ten corresponding to the crests. Velocity values of  $U_r$  and  $V_\theta$  corresponding to each phase instant defined by  $U_{ref}$  were sampled and averaged, respectively. In order to investigate periodic flow fields, a decomposition of velocity proposed by Hussain and Reynolds (1972) was adopted here, a time varying velocity  $u$  can be decomposed into a global mean component  $\bar{u}$ , a periodic mean component  $\tilde{u}$  and a random fluctuation component  $u'$ . This triple decomposition can be written as follows:

$$u = \bar{u} + \tilde{u} + u' \quad (1)$$

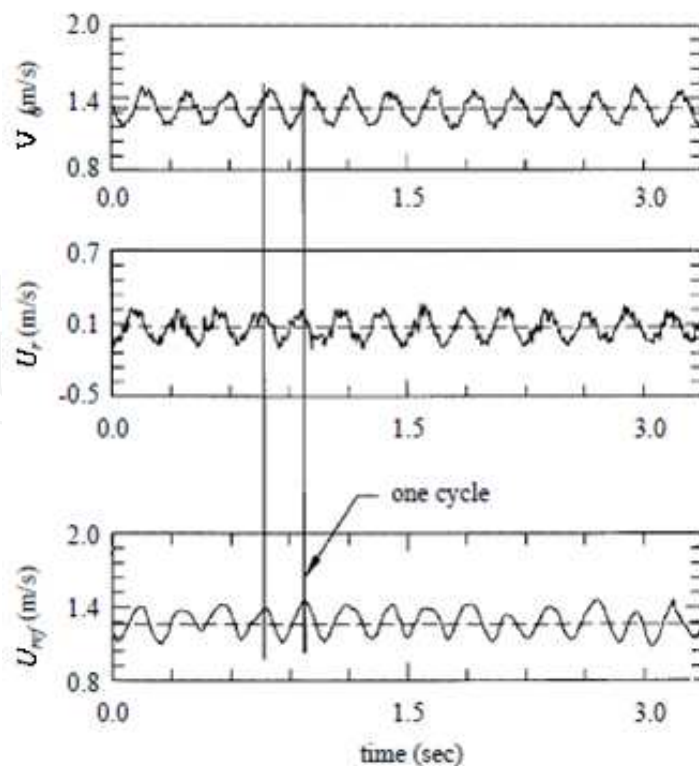


Fig. 3. Typical time records of the circumferential and radial velocity at  $r^*=0.40$

The bias of calculating global mean velocity was corrected by the method provided by McLaughlin and Tiederman (1973). In situ calibration was carried out with an oscilloscope and the maximum velocity bias was estimated to be less than 2%. Uncertainties of the phase-averaged velocity and Reynolds stresses were estimated statistically. The maximum uncertainty for phase-averaged velocity was about 4.5% at the 95% probability level. A typical value was about 1.2%.

### 3.1 PIV system

PIV is a non-intrusive technique for simultaneously measuring velocities at numerous points in a flow field. The fluid was seeded with tracer particles to illuminate the region under investigation. An image of the illuminated region was captured and then, a second image was taken shortly after. Appropriate analysis of these images produced an instantaneous velocity vector map. The PIV theory was introduced by Adrian (Adrian, 1984). At that time, due to hardware limitations, a single photographic frame was exposed numerous times and analyzed using an auto-correlation technique. However, enhanced photographic speed recording soon facilitated capturing separate frames for analysis using cross-correlation (Keane and Adrian, 1992). The cross-correlation technique is generally impractical for high-speed flows; the time interval between video frames is sufficiently long that any correlations between particle positions are lost (Willert, 1991). Auto-correlation, conversely, permits spacing of exposures as close as the light source allows without overlapped particle images.

The PIV system appears in Fig. 4 present the PIV system. For PIV measurements, double pulsed Nd:Yag lasers supplied the pulsed laser sheet (power, 170mJ/pulse) to illuminate the flow field being measured. Thus, the pulse duration and delay resolution were 50 ns. Each laser had a nominal repetition rate of 10Hz, and could emit double-pulsed lasers. Polycrystalline particles (particle diameter is about 30 $\mu$ m, density is 0.98 g/ml) were utilized as PIV tracers in the flow field. A Nikon F4 camera was employed to capture PIV images. A laser-sheet head, 1.5 mm thick, was mounted on an optical table, and generated a laser-light sheet that intersected the camera optical axis perpendicularly. The twin Nd:Yag lasers and camera were controlled via a synchronizer. The experimental system recorded 30 velocity fields per second. Each velocity field was obtained from a pair of consecutive images; the second image in the pair was captured 1ms after the previous image via a frame straddling approach. The PIV images captured by the camera were digitized by a scanner, and then transferred to a computer for image processing. The spatial resolution of the images was as high as 2400 $\times$ 1600 pixels.

The PIV image was transferred to a computer for gray scaling. The processed image with 256 gray levels was then divided into several small interrogation areas for quantifying the average particle displacement within each of them. The images were divided into 64 $\times$ 64 pixel interrogation areas, and 50% overlap grids were employed for the PIV image processing. Commercial software (TSI Insight) was used to process the PIV image and to compute the velocity vectors through the auto-correlation algorithm. Since the vortex structures or velocity reversals would not be presented in the laboratory frame, the velocity field could thus be calculated without directional ambiguity from a single double-exposed PIV image.

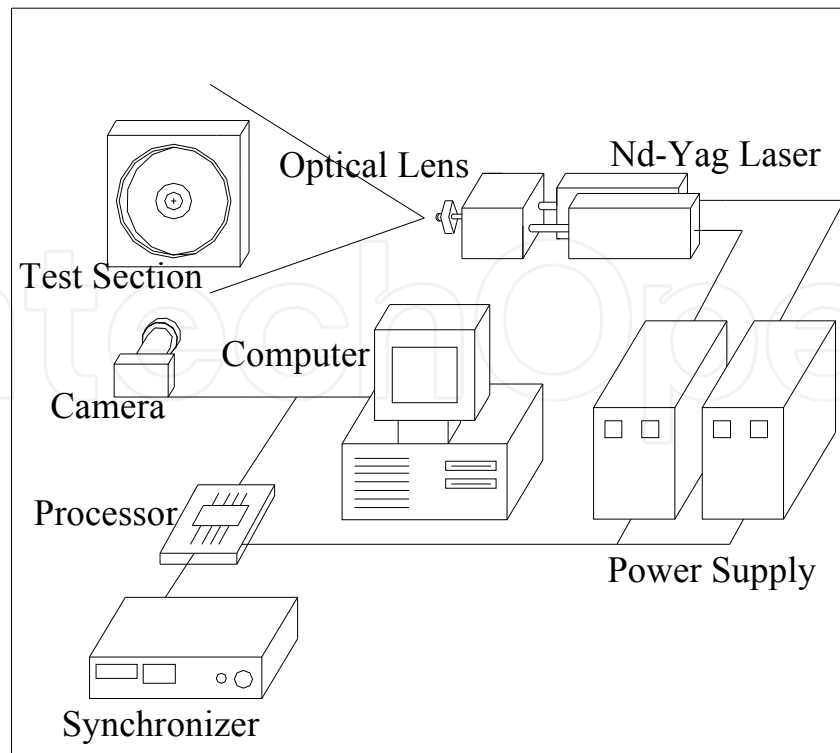


Fig. 4. Sketch of PIV experimental apparatus.

The accuracy of velocity measurements was estimated, depending on the ability to determine the displacement of a particle (Adrian, 1991). Here, a parabolic interpolation method was used to search for the peak of the autocorrelation function with sub-pixel accuracy, and hence the uncertainty of the vector-processing algorithm was reduced to 0.03 pixels. The time interval between two pulsed lasers was chosen to give the particle displacement of not less than 6 pixels, to keep a relative error below 0.5%. For a typical flow velocity of 1.5 m/s, this error corresponds to a velocity error of 70.75 cm/s. However, there are a number of other aspects in PIV measurements that can affect the accuracy of measurements due to imperfections in the apparatus, the particular PIV parameters used, and the nature of the flow being measured. In order to ensure the reliability of PIV measurements, a calibration based on the comparison of the measurement results of LDV and PIV was applied. Here, the time average of the instantaneous velocity measured by PIV was compared with the mean velocity measured by LDV. The deviation between two velocity data was found to be within 3%.

### 3.2 Flow visualization

Flow visualization was performed to confirm the flow field division identified by the velocity measurements. Fig. 5 presents the experimental apparatus for flow visualization in both the  $r-\theta$  plane and the  $r-z$  plane. To visualize the flow structure in the  $r-\theta$  plane, a flow visualization technique that displays particle distribution was used. Briefly, a light sheet generated by the laser from the Ar<sup>+</sup> system illuminated magnesium oxide particles. Particle diameter was 1.0 $\mu\text{m}$  and density was 1.5–5.5 g/ml, resulting in a Stokes number of  $10^{-6}$ . The particles were injected into the flow field adjacent to the hub using an injector

inserted through the enclosure. Near the hub where the flow was in solid body rotation, the particles accumulated and reflected the light sheet to illuminate the region. Away from the hub where the flow mixing rates were high, the few particles penetrating from the bright region were diluted rapidly.

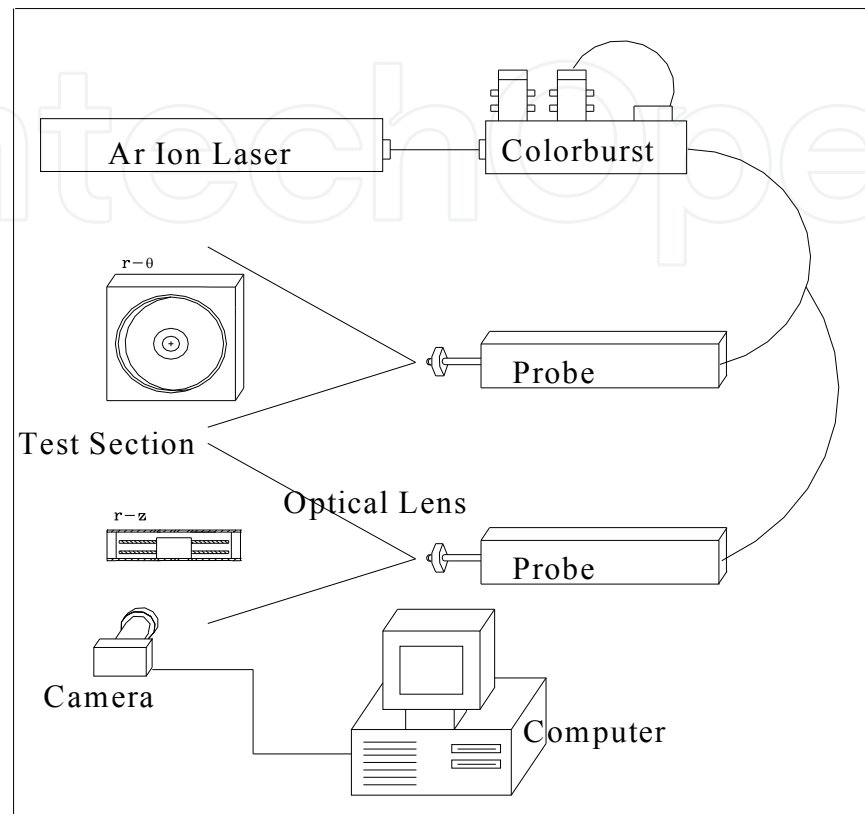


Fig. 5. Sketch of flow visualization experimental apparatus.

The flow visualization in the  $r-z$  plane emphasizes the region near the enclosure where the flow exhibits a complicated pattern. To visualize the above mentioned flow motion, Rhodamin B was injected near the enclosure. As a result, the fluid in this cross stream flow contained more dyes than the flow near the hub where the fluid was in solid body rotation around the hub center. When illuminated by the light sheet, the flow regions where the dyes were in abundance appeared bright and the near hub region appeared dark. With the concentrations used, this method might obtain the impressions of the cross-stream flow motion. A useful consequence of this method is that the different dye concentrations help one to distinguish between regions of different flow region.

## 4. Results and discussion

### 4.1 LDV measurement

#### 4.1.1 Mean velocity profiles

Fig. 6 shows the normalized mean circumferential velocity component measured as a function of the radial position along the symmetrical plane, midway between the two disks ( $z=0$ ). The mean values have been normalized by the local disk speed. A horizontal dashed

line was plotted to represent the local disk speed  $U/r\Omega=1$ . The dashed line manifests the solid body rotation. Fig. 6 shows that the velocity of the fluid begins to deviate from the solid body rotation at the position of about  $r^*=0.35$  in the present study. Included for comparison are also the results measured by Abrahamson and colleagues (1989) ( $Re=4.5\times 10^5$ ) and Tzeng and colleagues (1991) ( $Re=7.9\times 10^4$ ). The circumferential velocity begins to deviate from the solid body rotation at nearly the same dimensionless radial position of about 0.45 in the results measured by Abrahamson (1989) and Tzeng and their colleagues (1991). The difference is caused by the larger axial distance of the disks in the present work. The dimensionless axial distance in the other studies was fixed at  $S/D=0.05$ , whereas the value adopted in this study was  $S/D=0.12$ . The axial distance of the disks in the studies of Abrahamson (1989) and Tzeng (1991) and their colleagues was so small as to prevent the inflow with momentum deficit from penetrating a greater distance inside. For comparison, the experiments were also performed at  $S/D=0.05$ . As can be seen, good agreement can be found between the present results and those of Abrahamson (1989) and Tzeng (1991) and their colleagues.

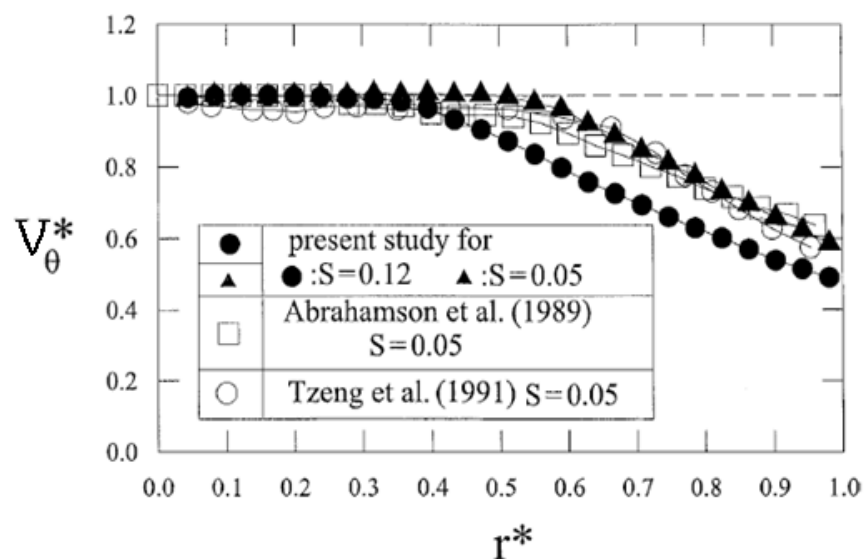


Fig. 6. Radial profiles of the circumferential mean velocity.

#### 4.1.2 Power spectra

Fig. 3 shows the measured time-resolved circumferential and radial velocities at the midplane between the two disks at  $r^*=0.395$ . These time sequences display distinct sinusoid-like oscillations. The Fourier spectra of radial and circumferential velocities at several radial positions were calculated. The results of radial and circumferential velocity power spectra were presented as examples in Fig. 7 and 8. The actual frequencies of the spectra were normalized by 0.75 times the disk rotational frequency. The spectral results show peaks in energy at an integral normalized frequency of  $f^*=3$ . Abrahamson and colleagues (1989) reported similar results. In addition to the spectral frequency, Fig. 7 shows

a plot of spectral intensity as a function of radial position. For radial velocity, the spectral intensity increases with  $r^*$  and reaches a maximum value at about  $r^*=0.47$ ; it then begins to decrease to as weak a value as  $r^*\sim 1$ . The radial velocity is most energetic at  $r^*\sim 0.5$ , and its spectral intensity displays good symmetry to  $r^*\sim 0.5$ .

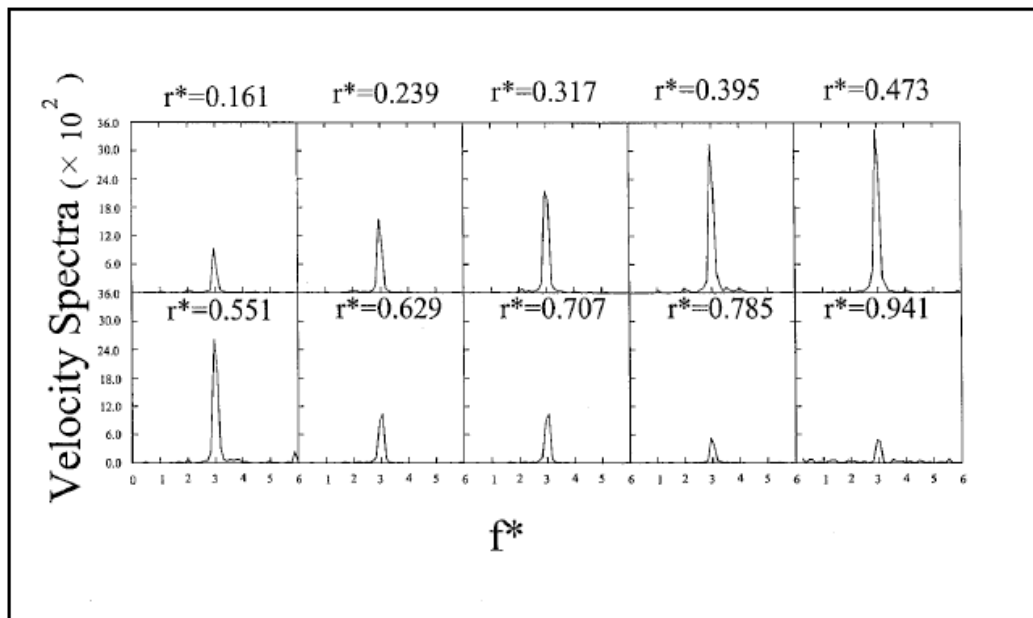


Fig. 7. Normalized spectra of circumferential velocity fluctuation at various radial positions.

It is to be noted that the distribution of spectral intensity for circumferential velocity (as shown in Fig. 8) is quite different from that of radial velocity. There are two local maximums of circumferential power spectra intensity. The first local maximum value takes place near the point  $r^*= 0.4$ . It is also the most energetic spot for circumferential velocity because the highest value of the circumferential spectral intensity arises there. It recalls the point at the interface of the inner and outer regions, as discussed previously. The second local maximum occurs at  $r^* = 0.72$ . It is located at the center of the vortical structure. Thus, it is clear that the circumferential velocities are more energetic at the interface of the inner and outer regions and also near the center of the vortical structure.

#### Streamline patterns at different phases

Fig. 9a shows the vector fields, and Fig. 9b shows the streamline patterns for one of the 10 phases, as observed with a  $0.75\Omega$  reference speed. Fig. 8 shows the streamline patterns as observed with a  $0.75\Omega$  reference speed. The streamline patterns at different phases during the passage of one vortex are demonstrated as an example. Some other reference speeds were also tested. The test results reveal that the vortical structure could not be recognized at a higher reference speed. On the contrary, the vortical structure is located in the solid-body rotation region at a lower reference speed. This phenomenon is obviously unreasonable. The appropriate rotational speed was found to be  $(0.75\pm 0.05)\Omega$  in the present case. A similar reference velocity was found by other researchers, such as Abrahamson and colleagues (1989). In their work, the camera was mounted on a motor that followed the rotation of the disks. The vortical structure could not be observed under a fixed-reference frame. Three distinct regions can be distinguished from the streamline patterns in Fig. 10.

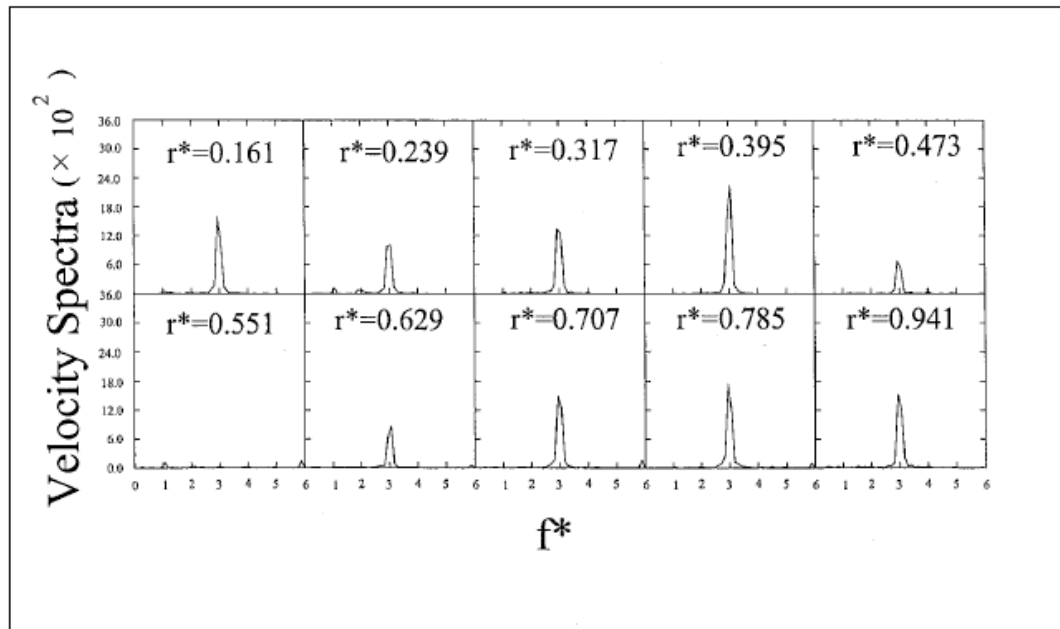


Fig. 8. Normalized spectra of circumferential velocity fluctuation at various radial positions.

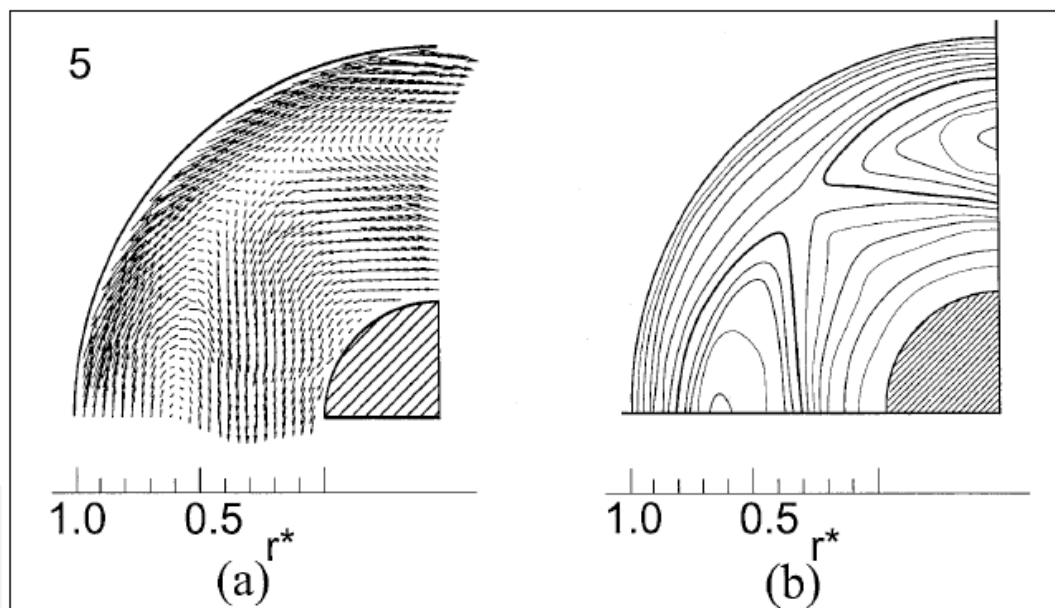


Fig. 9. Velocity vector and streamline patterns. (a) Velocity vector, observed at a reference velocity of  $0.75\Omega$ . (b) Streamline pattern, observed at a reference velocity of  $0.75\Omega$ .

The inner solid-body rotation region ranges from  $r^* = 0$  to  $0.35$ ; the outer vortical structure region from  $r^* \sim 0.35$  to  $0.9$ ; the shrouded boundary layer region from  $r^* = 0.9$  to  $1$ . It is noted that there seems to be no radial flow across the boundary between the rotating disks and the outsides of the disks, as shown in Fig. 10. However, because the centrifugal force acts on the rotating fluid, there must exist radial inflow and outflow. The inflow and outflow regions rotate in the same direction as the disks, forming a periodic flow field (Mochizuki, 1993). Extended experiments have been carried out in the cross stream ( $r$ - $z$ ) plane (Wu, 2000). The experimental results show that there is indeed radial flow. However, the circumferential

components are much larger than the radial ones, so the radial flow is not clearly observed from the phase-averaged measured data.

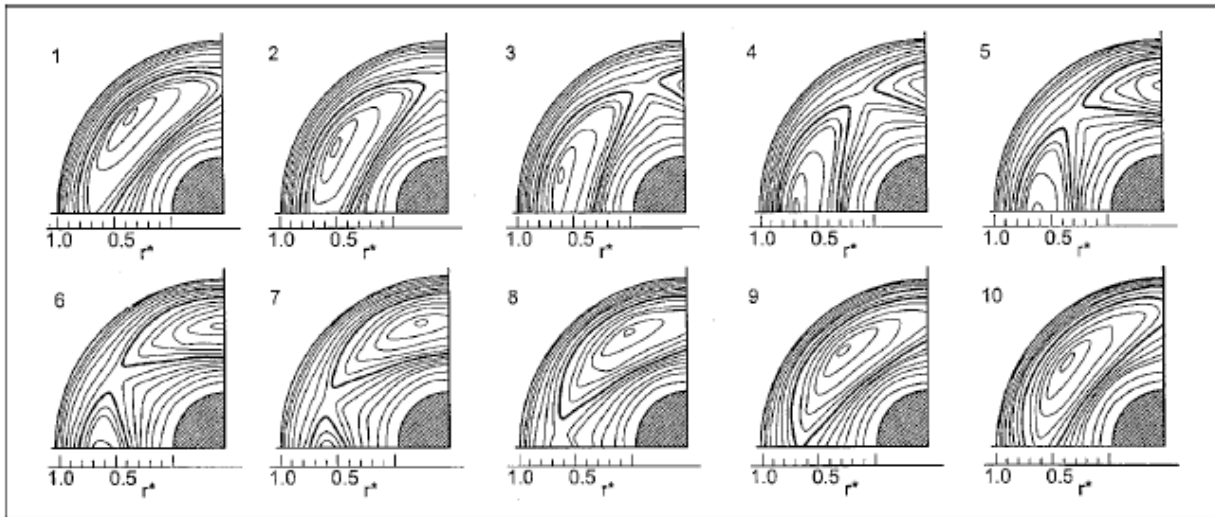


Fig. 10. The streamline patterns at various phases at a reference velocity of  $0.75\Omega$  and a contour interval of 0.2.

Although only a quarter of the frame was reconstructed, the number of the vortical structure can be easily determined to be 3. This integer is the same as the normalized frequency found in the power spectra analysis, as shown in Fig. 7 and 8. These findings demonstrate that the velocity oscillations result from the periodic passage of flow structure. The center of the vortex is located at  $r^* = 0.72$ . In addition, the radius of the inscribed circle of the vortical structure is found to be the same as that calculated by the formula  $R_i = R_2 (N - \pi A) / (N + \pi A)$ , as proposed by Tzeng and colleagues (1991), where  $\pi A = N - f_s / \Omega$ . The oscillatory frequency  $f_s$  measured is 9.9 Hz, and the number of the vertical structure  $N$  is 3 in the present study. The inscribed circle radius calculated by the formula is thereby  $R_i = 108.7$  mm. In Fig. 9, the inscribed circle of each phase was drawn to find its radius, and the average value of the 10 radii was taken. The inscribed circle of the polygonal structure with the average radius intersects the dimensionless radial position at  $r^* = (r - R_1) / (R_2 - R_1) = 0.4$ , corresponding to  $r = R_i = 110.7$  mm. There is little difference between the calculated and measured values.

#### 4.2 PIV measurement

Fig. 11(A)-1 presents the instantaneous velocity field at  $Re = 5.25 \times 10^5$  ( $\Omega = 133$  rpm and  $f_n = 2.22$  Hz). The radial velocity profile along  $\theta = 0^\circ$  is found to increase with increasing  $r$  (from the hub) until about  $r^* = 0.5$  and then decrease near the shroud. The fluids within  $r^* = 0.5$  are primarily moved by the rotating disks. Beyond  $r^* = 0.5$ , shroud shear stress increases gradually and, hence, impacts fluid velocity. No structure would be found in the laboratory frame (Fig. 11(A)-1). By subtracting a reference velocity from the original circumferential velocity, a rotating reference frame is simulated to reveal the vortex structure. The camera frame rate is controlled to identify the reference velocity. When the frame rate is 1.66 Hz (75% of the disk rotation rate) and reference velocity is  $0.75\Omega$ , the

motion of vortex structure is frozen, i.e., the vortex in sequence pictures are almost on the same rotation phase.

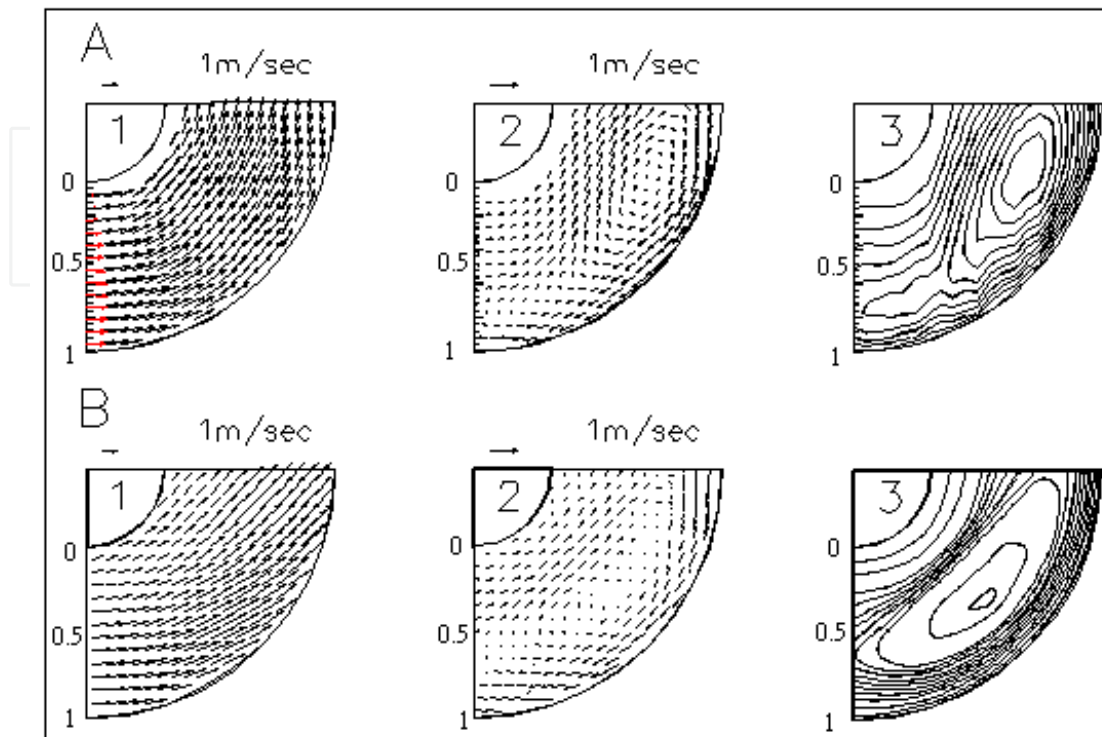


Fig. 11. Procedure for reconstructing the flow patterns with a simulated rotating reference frame. Stream line pattern A : PIV , B : LDV.

Above results demonstrates that the vortex structure rotates at 75% of disk rotation velocity and can be observed correctly by an observer moving at this reference velocity. Fig. 11(A)-2 presents the velocity field with this reference frame. Then Fig 11(A)-3 presents the streamlined pattern of the reference frame obtained by integrating results (as Fig. 11(A)-2). The inner flow region surrounding the hub is a polygon shape. Beyond the inner region is the outer region containing circumferentially periodic large-scale vortex structures.

Abrahamson et al. (1991) also identified an outer region that is dominated by large-scale vortex structures. These structures are almost evenly distributed around a circle, approximately two-thirds of the distance between the hub and the shroud, and generally span the radial of the outer region. Here, the rotating reference velocity is set at 70–80% of the disk rotation speed, and a reference velocity higher or lower than 70–80% of the disk rotation speed would cause the vortex center to deviate from the radial location again.

To exhibit the periodic variation characteristics of the flow, the measured data was processed using the phase averaged method(Eq.1). Fig. 11(B)-1 shows the processed velocity field. The principle associated with method was utilized by Wu and Chen (2002). Fig. 11(B)-3 presents the integrated streamline pattern for the rotating reference frame.

Although the grid finenesses in Fig. 11(A)-3 and Fig. 11(B)-3 are similar, the streamlines in Fig. 11(B)-3 are smoother. Moreover, unlike the results for the phase-averaged LDV measurements that reveal a symmetrical vortex (Fig. 11(B)-3), the vortex front revealed by

PIV measurements has the shape of an arc with a pointed rear section. Fundamentally, LDV is a point measurement technique. When combined with a phase average process, LDV can obtain the global mean and periodic mean components ( $u = \bar{u} + \tilde{u}$ ), and generally not the fluctuation term ( $u'$ ) if the data rate in a cycle is not sufficiently high. The vortex identified by PIV measurements acquires the vortex structure; whereas its irregular shape exhibits the perturbation of instantaneous velocity.

Appropriate PIV measurements can obtain the complete and instantaneous velocity components and, hence, provide the real flow information. To acquire the whole field velocity by LDV, time-consuming point-by-point measurements are required. Moreover, an additional laser is required to freeze the flow using a phase-averaging method and, hence, measuring work becomes extremely complicated. However, PIV can measure the whole field velocity effectively. Additionally, time resolved PIV measurements can be achieved by controlling the camera frame rate; an advantage cannot be realized with LDV.

#### 4.3 Flow visualization-the $r-\theta$ plane

The flow visualization photograph taken at the instant before the particles injected near the hub diffuse uniformly and streamlines constructed from measured velocity vector field are depicted in Fig. 12. Note that in flow visualization particles are injected once and the injector is then removed. After several seconds, the particles diffuse to fill the inner region. The flow visualization image in the  $r-\theta$  plane clearly reveals two regions. The existence of a partition between the inner and outer regions is verified by the accumulation of most particles in the inner region for several minutes. The inner region is bright as the particles bounded there strongly reflect the illuminating light. Beyond the inner region, only few particles exist and have a diffuse, grainy distribution. The triangular boundary of the inner

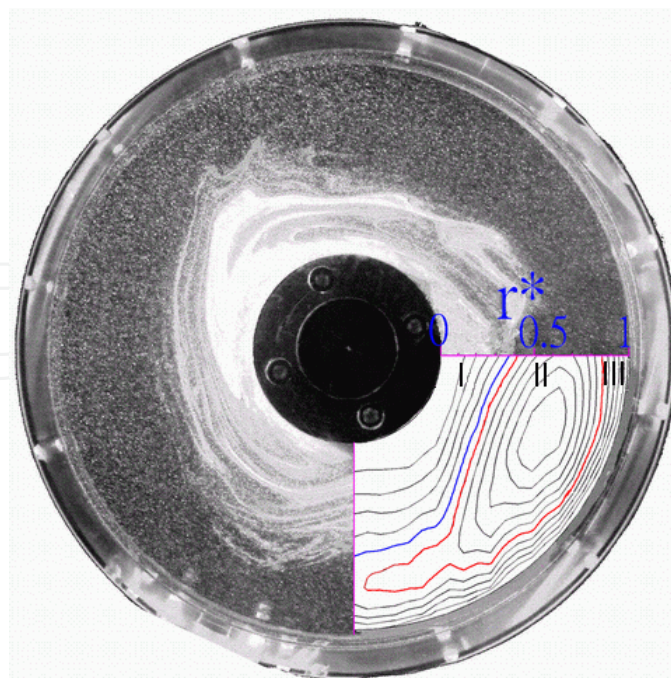


Fig. 12. Flow visualization photograph and stream line in the  $r-\theta$  plane ( $Re = 5.25 \times 10^5$ ,  $S=0.09$ ).

region rotates at a speed slightly slower than the disks. Furthermore, the radius of the inscribed circle of the triangle intersects the radial coordinate axes at about  $r^*=0.39$ . Fig. 11(A)-3 is also inserted on the right lower corner of Fig. 12. It is seen that for the present co-rotating disk flow, periodic vortex structures rotate at about 75% of disk rotation speed. Consequently, the outer region and shroud region can be identified.

The above flow visualization is performed to verify the division of the flow field based on PIV measurements. Based on the reconstructed flow patterns obtained by PIV and flow visualization (Fig. 12), the flow field is divided into three regions: (I) inner region (solid body rotation region) ( $0.04 < r^* < 0.39$ ); (II) outer region (vortex region) ( $0.39 < r^* < 0.75$ ); and, (III) shroud region ( $0.75 < r^* < 1$ ).

#### 4.4 Flow visualization-the $r-z$ plane

The flow visualization in the  $r-z$  plane is also conducted. In Fig. 13(A), due to the solid body rotation, the injected dyes can not penetrate near the hub, resulting in a dark solid body region (Fig. 13(C) sub-region 1<sup>st</sup>). When illuminated by the light sheet, the boundary layers (Fig. 13(C) sub-region 4<sup>th</sup>) on both the upper and lower disk surfaces are clearly observed. The fluids from the boundary layers are redirected in the axial direction adjacent to the enclosure wall, and hence cause a thin shroud shear layer (Fig. 13(C) sub-region 8<sup>th</sup>) on the wall surface. These two axial flows collide and merge on the enclosure wall, and they are subsequently pumped radically inward by the adverse pressure gradient force. In order to balance the mass flux, the Ekman layer (Fig. 13(C) sub-region 6<sup>th</sup>) is induced to replace the outward flow through the boundary layers and hence maintain the cross-stream circular flow (Fig. 13(C) sub-region 5<sup>th</sup>). As a result, an axial flow layer appears slightly outer than the solid body region and spans the distance between two disks. This flow layer is designated as a detached shear layer (Fig. 13(C) sub-region 3<sup>rd</sup>) resulting from the different rotations in the solid body region and in the Stewartson flow region (Fig. 13(C) sub-region 7<sup>th</sup>). The flow field in the  $r-\theta$  plane can be divided into three regions. The radial extents of these three (I || III) regions are also indicated in the top of Fig. 13(C) in order to make a comparison of the flow regions in the  $r-\theta$  plane with the regions in the  $r-z$  plane.

#### 4.5 Velocity distribution

Fig. 13(B) shows the normalized radial and circumferential velocity distribution at different radial positions respectively. The flow performs solid body (region I; Fig. 13(C) sub-region 1<sup>st</sup>) rotation between  $r^*=0.04$  and  $r^*=0.39$ , as can be easily seen. The boundary layer (Fig. 13(C) sub-region 4<sup>th</sup>) starts to grow at  $r^*=0.39$  and develop gradually along the radial direction toward the shroud. At this moment, note that the fluid in this flow is dominated by the rotating centrifugal force, adverse pressure caused by the static shroud and the Coriolis force induced by the rotation of these two forces. Within the interface between inner and outer regions, the fluid is first affected by adverse pressure force and is no longer subject to solid-body rotation. The above mentioned three forces affect the flow obviously. The fluid is first dragged by the Coriolis force to flow toward the face of disk. Then, the fluid near the disk affected by the centrifugal force flows radically outward and hence forms the boundary layer there. Since the centrifugal force grows along the radial direction, the boundary layer also becomes thicker, as shown in Figs. 13(A) and 13(B). However, within the

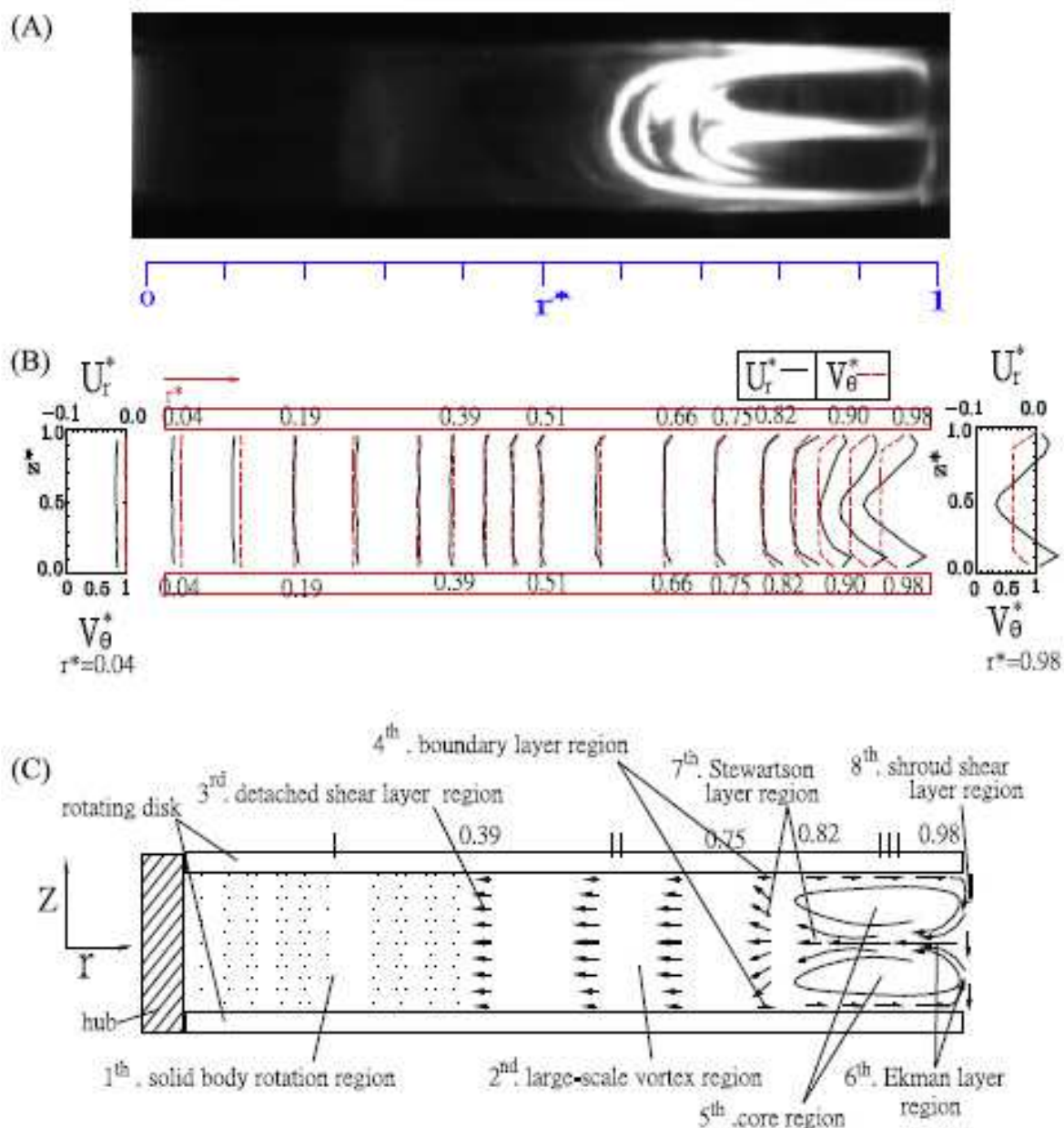


Fig. 13. (A) Flow visualization, (B) velocity distribution (LDV), and (C) sketched characteristics and divisions of flow field in the  $r-z$  plane ( $Re = 5.25 \times 10^5$ ,  $S=0.09$ ).

region very close to the shroud ( $r^*=0.98$ ), the adverse pressure induced by static shroud strongly impacts the flow. The centrifugal force causes the fluid along the disk to flow outward, while the adverse pressure causes the fluid placed in the middle of two disks to flow inward. The imbalance of these two forces creates two symmetric circular flow (Fig. 13(C) sub-region 5<sup>th</sup>) appearing near the shroud. In the flow field, the circumferential flow velocity is much higher than the radial one, hence, the radial extent where the fluid backflow from the shroud is restricted to be near the shroud and within the region where the adverse pressure can affect (about beyond  $r^*=0.75$ ). This region ( $0.75 < r^* < 1.0$ ) within which the influence of boundary effect is obvious is referred to as shroud region (region III). In the  $r-z$  plane, experimental results indicate the flow structure can be divided into six sub-regions.

#### 4.6 Integrating each plane results

According to the PIV measured velocity field, flow visualization and the prior LDV measured velocity field, the flow between disks can be identified into three regions which in fact consist of eight sub-regions. The flow patterns are sketched in Fig. 13(C), and each sub-region is described respectively as follow:

- i. **Inner region** ( $0.04 < r^* < 0.39$ ): The dimensionless circumferential velocity remains constant and the flow performs **solid body rotation**. (solid body rotation region also is sub-region 1<sup>st</sup>)
- ii. **Outer region** ( $0.39 < r^* < 0.75$ ): The dimensionless circumferential velocity declines radially outward and the **large-scale vortex** structures are observed in this region (the vortex structure is sub-region 2<sup>nd</sup>). Within the vortex region, there are boundary layers on the face of both disks. The **detached shear layer region** (sub-region 3<sup>rd</sup>) resides between the solid body rotation region and the vortex region. The **boundary layer region** (the boundary layers on both disks are the sub-region 4<sup>th</sup>) starts at  $r^*=0.39$  on the disk surface and gradually develops to the disk edge.
- iii. **Shroud region** ( $0.75 < r^* < 1$ ): The flow is three-dimensional in this region. In the core of the flow field, the fluids flow inward by the adverse pressure gradient and induce a pair of circular flow. The core region is the sub-region 5<sup>th</sup>, which contains both the upper and lower circular flow, but not includes the other parts of the circular flow. The sub-region which is not inclusive in sub-region 5<sup>th</sup> is the Ekman layer region (sub-region 6<sup>th</sup>). The circular flow structure acts like an annular chain to surround the outer-region vortex. As the result, the vortex would not be flung out of the outer region by the centrifugal force, and hence cause the vibration of the whole flow field. The Stewartson layer region (sub-region 7<sup>th</sup>), where three vortices compromise mutually, locates between the vortex region and the shroud boundary-layer region. Besides, the shroud shear layer region (sub-region 8<sup>th</sup>) lies between disk edge and shroud. In addition, the circumferential velocity (Fig. 13(B)) component in the 5<sup>th</sup> core region reveals that a pair of circular flow structure acts like an annular chain to surround the 2<sup>nd</sup> sub-region large-scale vortex. This finding is also not reported in the literature. Among these sub-flow regions the 5<sup>th</sup> to 7<sup>th</sup> flow regimes are not identified previously.

#### 4.7 The phase velocity

Fig. 14 presents normalized mean circumferential velocity (marked with ●) distribution along the radial direction on the mid-plane measured by PIV. The flow field is easily divided into two regions. First, the normalized mean circumferential velocity remains about 1, from  $r^*=0$  to  $r^*=0.39$ . This region is the solid body rotation region. Second, from the location  $r^*=0.39$  to  $r^*=0.98$ , the normalized mean circumferential velocity decreases from 1 to approximately 0.54. Abrahamson et al. (1989), who performed a similar study, defined the first region as the inner region and the second region as the outer region.

At this point it should be mentioned that the vortex structures rotate at 75% of the angular velocity of the disks (mentioned in the Introduction), and the disk rotating period  $\Omega$  is 133rpm. By controlling the camera frame rate, the phase-resolved PIV measurement is achieved. Here, the velocity fields at different phases are measured and the camera time

interval is set at 1/15 of the vortex structure rotation period. (A vortex is divided into 5 phases). A synchronizer controls the laser repetition rate and camera frame rate. However, the camera cannot take repeated images using such a short interval. To achieve this sampling interval, the trigger time is shifted one period for each run.

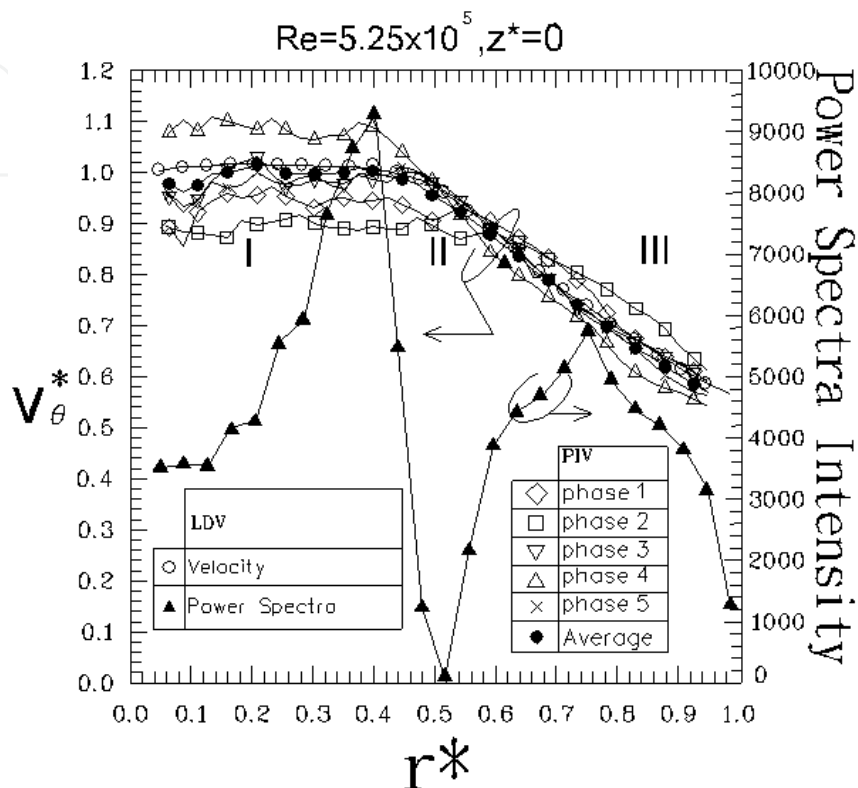


Fig. 14. PIV measured radial profiles of the circumferential phase velocity and LDV measured power spectra.

Fig. 14 shows the radial profiles of velocity from the hub to the shroud under the same time interval and along the same radial position ( $\theta=0$ ). The normalized velocity near the hub has a small range of perturbations in the radial direction. The fluid is dominated by rotating centrifugal force, adverse pressure caused by the static shroud and the Coriolis force. At the interface between inner and outer regions, the fluid starts to be influenced by the adverse pressure force and leaves solid-body rotation. Boundary layers develop along the surface of each disk beyond the solid body region. Fluid in the boundary layer is pumped radially outward by a combination of centrifugal force and Coriolis force.

Experimental data indicates that at a certain radial location, the normalized circumferential velocity begins declining. However, the locations of the normalized circumferential velocity begin declining at different time steps. Based on above result, the polygon inner region is compressed by the vortices. When the vortex center moves toward the sampling line ( $\theta=0$ ), the boundary of inner region is flattened inward toward the hub. Therefore, the normalized circumferential velocity near the hub arises as a result of the reducing channel. Conversely, when a vortex leaves the sampling line, the velocity near the hub continually

declines due to the expanding inner region. As indicated by the velocity profile labeled with a  $\Delta$  in Fig. 14, a vortex center bypasses the sampling line, and the normalized circumferential velocity remains larger than 1 as it moves from the hub outward to  $r^* = 0.39$ . Contrary to this, as the inner region vortex bypasses the sampling line (profile labeled with a  $\square$ ), the normalized circumferential velocity is slightly less than the disk speed and maintains its value until  $r^* = 0.60$ .

The periodic passage of the vortex structure affects the normalized circumferential velocity (Fig. 14). The velocity profiles rise or fall at different time steps, and the increases and decreases in the inner and outer regions are opposed to each other. When the vortex center moves close to the sampling line ( $\theta = 0^\circ$ ), the inner region boundary is flattened inward toward the hub. Therefore, the normalized circumferential velocity near the hub arises due to the reducing channel and increases continually. Until the vortex center arrives, the dimensionless circumferential velocity peaks. Conversely, when a vortex leaves the sampling line, the velocity near the hub continually decreases due to the expanding inner region. In the outer region, fluid velocity increases or decreases periodically in a manner that is opposite to that in the inner region.

However, this flow behavior was not observed with the LDV-measured velocities (marked with a  $\circ$ ) (Wu and Chen 2003). The fluid in the inner region coincides with rotating disk speed. The radial location at which velocity starts to decline is fixed at  $r^* = 0.39$ . The mean velocity profile measured by LDV is in agreement with the global mean velocity profile measured by PIV (marked with a  $\bullet$ ). Experimental data indicate that LDV measurement can only show time-averaged results, and cannot exhibit the periodic perturbation of velocity.

#### 4.8 Power spectra

The velocity time history recorded by LDV is also utilized for power spectrum analysis. Two local maxima of spectral intensity can exist (Fig. 14). The first maximum is located at  $r^* = 0.39$ , whereas the second local maximum is at  $r^* = 0.75$ , indicating that circumferential velocity has increased energy at these two locations. Notably, the spectral intensity is almost zero at  $r^* = 0.51$ , implying that circumferential velocity does not oscillate at this location.

The normalized mean circumferential velocity starts declining at  $r^* = 0.39$  (Fig. 14). Instantaneous velocity profiles also indicate that this location is sometimes in the inner region, and sometimes in the outer region. Consequently, the radial gradient of velocity varies markedly, and the velocity value changes periodically due to passing vortices. The radial gradient of velocity also varies violently at about  $r^* = 0.7$ , the location of vortex center. When a vortex passes the sampling line, its self-rotation causes the fluids at each side of the vortex center to accelerate in opposite directions, resulting in strong variation in radial gradient velocity. Furthermore, as the vortex passes or leaves the sampling line, the velocity value also varies periodically. Notably, the profiles of velocities intersect at about  $r^* = 0.51$ , where spectra intensity approaches zero. Comparatively, at the position where spectra intensity achieves a maximal value, the amplitudes of velocity change significantly.

Power spectra analysis provides periodic information, such as the distribution of spectra intensity and the primary flow frequency, as long as the grids of LDV measurements are adequately refined. However, spectra intensity distribution cannot be explained effectively

by the global mean velocity profile measured by LDV. The phase velocity measurements provide the physical explanation of the cyclic variation in the 1st solid body rotation region reported previously by LDV.

## 5. Conclusions

Six major conclusions may be drawn.

1. By using two laser Doppler velocimeters and the phase averaged method, the temporal vortical structure in the flow between corotating disks can be quantitatively reconstructed. The detailed flow information, including the mean, periodic, and random terms, provides a basis for numerical verification.
2. The power spectral analysis shows that all the peaks in the energy are at the same integral normalized frequency. The value of the normalized frequency is the same as the number of the vortical structure observed in the reconstructed streamline patterns. This indicates that the flow oscillations result from the periodic passage of the flow structure.
3. Both laser (LDV, PIV) measurements and flow visualization in the  $r-\theta$  plane show that the flow feature between the co-rotating disks can be divided into three regions: (I) Inner region: solid body rotation region ( $0.04 < r^* < 0.39$ ), (II) Outer region: vortex region ( $0.39 < r^* < 0.75$ ), and (III) Shroud region: shroud shear layer region ( $0.75 < r^* < 1$ ). Among them the shroud region is quantitatively identified for the first time.
4. In the  $r-z$  plane, the flow structure is found to consist of six sub-flow regions. Combining the flow patterns in the  $r-\theta$  and  $r-z$  planes, the complex 3-D flow explored can be divided into eight sub-regions, namely 1<sup>st</sup> solid body rotation region, 2<sup>nd</sup> large-scale vortex structure region, 3<sup>rd</sup> detached shear layer region, 4<sup>th</sup> boundary layer region, 5<sup>th</sup> core region, 6<sup>th</sup> Ekman layer region, 7<sup>th</sup> Stewartson layer region, and 8<sup>th</sup> shroud shear layer region. The (5<sup>th</sup> to 7<sup>th</sup>) three sub-flow regions are identified in the present study.
5. The large-scale vortex structure is not flung out of the above-mentioned 2<sup>nd</sup> sub-region by the centrifugal force since the circular-pair flow structure in the core region acts like an annular chain to surround it.
6. The periodical variation of circumferential velocity or the cyclic variation of the inner solid body rotation reported previously by authors' LDV spectra results can be explained by the present PIV phase velocity measured results.

## 6. Acknowledgement

There are so many thanks for the Department of Mechanical Engineering National Taiwan University of Prof. Yau-Ming Chen, who has had the long-term support and assistance to my papers. And also thanks for the subvention from National Science Council.

## 7. Nomenclature

a	Clearance between disks and shroud (mm)
D	Displacement between disks (mm)
$f^*$	Normalized frequency
$f_n$	Natural frequency of flow (Hz)
$f_s$	Dominant frequency of power spectra (Hz)
$f_n$	Natural frequency of flow (Hz)

N	Number of vortices
$R_1$	Radius of hub ( mm)
$R_2$	Radius of disk ( mm)
$R_3$	Radius of shroud (mm)
$R_i$	Radius of inscribing circle of polygon structure
Re	Reynolds number, $R_2\Omega/\nu$
r	Radial coordinate (mm) (mm) (mm) (mm)
$r^*$	$(r - R_1)/(R_2 - R_1)$
S	$D/R_2$
$U; u$	Velocity(mm/s)
$U_r$	Radial velocity (mm/s)
$U_{ref}$	Circumferential velocity of the reference point(mm/s)
$U_r^*$	Normalized radial velocity $U_r/r\Omega$
$V_\theta$	Circumferential velocity (mm/s)
$V_\theta^*$	Normalized circumferential velocity $V_\theta/r\Omega$
$\bar{u}$	Global mean of u
$\tilde{u}$	Periodic fluctuation away from $\bar{u}$
$u'$	Random fluctuation away from $\tilde{u}$
z	Axial coordinate (mm)
$z^*$	$z/D$

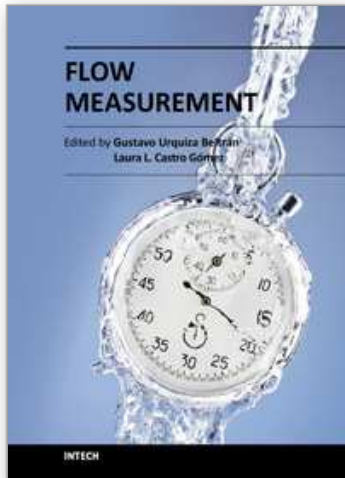
## 8. Greek symbols

$\Omega$	Rotating velocity of disk (rpm)
$\theta$	Periphery coordinate (degree)
$\nu$	Kinematic viscosity ( $\text{mm}^2/\text{s}$ )

## 9. Reference

- Abrahamson, S. D., Eaton, J. K., and Koga, D. J., The Flow between Shrouded Corotating Disks, *Phys. fluids A*, 1 (1989)241-251.
- Abrahamson, S. D., Koga, D. J., and Eaton J. K., Flow Visualization and Spectral Measurements in a Simulated Rigid Disk Drive, *IEEE Trans. Comp. Hybrids and Manuf. Tech.*, 11(4) (1988)576-584.
- Abrahamson, S. D., Eaton, J. K., and Chang, C., Flow Structure in Head-Disk Assemblies and Implications for Design, *Adv. Info. Storage Syst.*, 1(1991)111-132.
- Adrian, R. J., Image shifting technique to resolve directional ambiguity in double-pulsed velocimetry, *Applied Optics*, 25 (1986)3855-3858.
- Adrian, R.J., Particle-imaging Techniques for Experimental Fluid Mechanics, *Annu. Rev. Fluid Mech.*, 23(1991)261-304.
- Adrian, R. J., and Yao, C. S., Development of Pulsed LASER Velocimetry (PLV) for Measurement of Turbulent Flow, In *Proc. Symp. Turbul.*, ed. X. Reed, G. Patterson, J. Zakin, Rolla: Univ. No. 380 (1984) 170-186.
- Chang, C.J., Humphrey, J.A.C., and Greif, R., Calculation of Turbulent Convection Between Corotating Disks in Axisymmetric Enclosures, *Int. J. Heat Mass Transfer*, 33 (1990)2701-2720.

- Chang, C. J., Schuler, C. A., Humphrey J. A. C., and Greif R., Flow and Heat Transfer in the Space between Two Corotating Disks in an Axisymmetric Enclosure, *J. of Heat Transfer*, 111 (1989) 625-632.
- Herrero, J., Giralt, F., and Humphrey, J. A. C., Influence of the Geometry on the Structure of the Flow between a Pair of Corotating Disks, *Phys. of Fluids*, 11 (1999)88-96.
- Humphrey, J. A. C., Chang, C. J., Li, H. and Schuler C. A., Unobstructed and Obstructed Rotating Disk Flows: A Summary Review Relevant to Information Storage Systems, *Adv. Info. Storage Syst.*, 1(1991)79-110.
- Humphrey, J. A. C., and Gor, D., Experimental Observation of an Unsteady Detached Shear Layer in Enclosed Corotating Disk Flow, *Phys. Fluids*, 5(1993) 2438-2442.
- Humphrey, J. A. C., Schuler C. A., and Weber, D. R., Unsteady Laminar Flow Between a Pair of Disks Corotating in a Fixed Cylindrical Enclosure, *Phys. Fluids*, 7(1995)1225-1240.
- Hussain, A.K.M.F. and Reynolds, W.C., The Mechanics of an Organized Wave in Turbulent Shear Flow. Part 3. Theoretical Models and Comparisons with Experiments," *J. Fluid Mech.*, 54(1972)263-288.
- Iglesias, I., and Humphrey, J. A. C., Two- and Three-Dimension Laminar Flows Between Disks Co-rotating in a Fixed Cylindrical Enclosure, *Int. J. Numer. Meth. Fluids*, 26, (1998)581-603.
- Keane R.D., and Adrian, R.J., Theory of cross-correlation of PIV images, *Applied Scientific Research*, 49 (1992)191-215.
- Lennemann, E., Aerodynamic Aspects of Disk Files., *IBM J. Res. Develop.*, 18(1974)480-488.
- Perry, A. E. and Watmuff, J. H., The Phase-Averaged Large-scale Structures in Three Dimensional Turbulent Wakes, *J. Fluid Mech.*, 103(1981)33-51.
- Randriamampianina, A., Schiestel, R., and Wilson, M., Spatio-temporal Behavior in an Enclosed Corotating Disk Pair, *J. Fluid Mech.*, 434 (2001)39-64.
- Schuler, C. A., Usry W., Weber, B., Humphrey, J. A. C. and Greif, R., On the Flow in the Unobstructed Space between Shrouded Corotating Disks, *Phys. Fluids* , 2 (1990)1760-1770.
- Stewartson, K., On the Flow between Two Rotating Coaxial Disks, *Proc. Camb. Phil. Soc.*, 3(1953)333-341.
- Szeri, A.Z., Schneider, S.J., Labbe, F. and Kaufamn, H.N., Flow between Rotating Disks (Part 1, Basic Flow), *J. Fluid Mech.*, 34(1983)103-132.
- Tzeng, H. M., and Humphrey, J. A. C., Corotating Disk Flow in an Axisymmetric Enclosure with and without a Bluff-body, *Int. J. Head and fluid flow*, 12(1991) 194-201.
- Willert, C. E., and Gharib, M., Digital Particle Image Velocimetry, *Exp. in Fluids*, 10 (1991) 181-193.
- Wu, S. C., The flow between corotating disks with/without an obstruction in a cylindrical enclosure, Ph.D. diss., National Taiwan University, 2000.
- Wu, S.C., and Chen, Y.M., Phase-Averaged Method Applied to Periodic Flow between Shrouded Corotating Disks, *International Journal of Rotating Machinery*, 8 (2002) 413-422.
- Wu, S.C., and Chen, Y.M., The Dynamic Behavior of the Coherent Flow between Shrouded Co-rotating Disks, *Journal of the Chinese institute of engineers*, 26 (2003) pp. 47-56.
- Wu, S.C., Tsai ,Y.S., Chang, Y.M. and Chen, Y.M., Typical Flow between Enclosed Corotating Disks and its Dependence on Reynolds Number, *Journal of the Chinese institute of engineers*, 29 (2006) 841-850.
- Wu, S.C., A PIV Study of Co-rotating Disks Flow in a Fixed Cylindrical Enclose, *Experimental Thermal and Fluid Science*, 33(2009), 875-882.



## **Flow Measurement**

Edited by Dr. Gustavo Urquiza

ISBN 978-953-51-0390-5

Hard cover, 184 pages

**Publisher** InTech

**Published online** 28, March, 2012

**Published in print edition** March, 2012

The Flow Measurement book comprises different topics. The book is divided in four sections. The first section deals with the basic theories and application in microflows, including all the difficulties that such phenomenon implies. The second section includes topics related to the measurement of biphasic flows, such as separation of different phases to perform its individual measurement and other experimental methods. The third section deals with the development of various experiments and devices for gas flow, principally air and combustible gases. The last section presents 2 chapters on the theory and methods to perform flow measurements indirectly by means on pressure changes, applied on large and small flows.

### **How to reference**

In order to correctly reference this scholarly work, feel free to copy and paste the following:

Shen-Chun Wu (2012). The LDV and PIV Study of Co-Rotating Disks Flow with Closed Shroud, Flow Measurement, Dr. Gustavo Urquiza (Ed.), ISBN: 978-953-51-0390-5, InTech, Available from: <http://www.intechopen.com/books/flow-measurement/the-ldv-and-piv-study-of-co-rotating-disks-flow-with-closed-shroud>

**INTECH**  
open science | open minds

### **InTech Europe**

University Campus STeP Ri  
Slavka Krautzeka 83/A  
51000 Rijeka, Croatia  
Phone: +385 (51) 770 447  
Fax: +385 (51) 686 166  
[www.intechopen.com](http://www.intechopen.com)

### **InTech China**

Unit 405, Office Block, Hotel Equatorial Shanghai  
No.65, Yan An Road (West), Shanghai, 200040, China  
中国上海市延安西路65号上海国际贵都大饭店办公楼405单元  
Phone: +86-21-62489820  
Fax: +86-21-62489821

© 2012 The Author(s). Licensee IntechOpen. This is an open access article distributed under the terms of the [Creative Commons Attribution 3.0 License](#), which permits unrestricted use, distribution, and reproduction in any medium, provided the original work is properly cited.

IntechOpen

IntechOpen